PREPARED FOR SUBMISSION TO JINST

The Wendelstein 7-X phase contrast imaging diagnostic

Z. Huang[1] **E. Edlund**[2] **M. Porkolab**[1] **J-P. Bähner**[3] **L.-G. Böttger**[3,4] **C. v. Sehren**[3] **A. von Stechow**[3] **O. Grulke**[3,4]

[1]*MIT Plasma Science and Fusion Center, Cambridge, MA 02139, USA*
[2]*SUNY Cortland, Cortland, NY 13045, USA*
[3]*Max Planck Institute for Plasma Physics, 17491 Greifswald, Germany*
[4]*Technical University of Denmark, 2800 Kongens Lyngby, Denmark*

E-mail: zjh@psfc.mit.edu

ABSTRACT: A phase contrast imaging (PCI) diagnostic has been developed for the Wendelstein 7-X (W7-X) stellarator. The PCI diagnostic provides a line-integrated measurement of turbulent electron density ïňĆuctuations, which is essential for understanding high performance scenarios that can lead to improved confinement at fusion-relevant temperatures and densities. The PCI system is also sensitive to coherent ïňĆuctuations, which arise from Alfvén eigenmodes or other MHD activity. This paper provides an overview of the hardware and the optical system and presents an example PCI measurement from the W7-X OP1.2b experimental campaign.

KEYWORDS: Only keywords from JINST's keywords list please

Contents

1 Introduction

Wendelstein 7-X (W7-X) is the largest optimized stellarator in the world, designed to create a reactor-relevant plasma under steady-state conditions. One of the major optimization criteria is the reduction of the neoclassical transport compared to classical stellarators [1]. First strong evidence of this has been obtained in the second operation campaign which introduced a carbon divertor, wall passivation by boronization and neutral beam injection (NBI) heating [2] in addition to the existing electron cyclotron heating (ECRH). The observed plasma confinement of heat and particles is indeed to a large extent dominated by turbulent transport [3]. Similar to the situation observed in tokamaks, turbulent transport is altered in W7-X when the central plasma density is peaked, which has been achieved by central plasma fueling either by hydrogen pellet injection or NBI fueling [4]. In these kind of discharges, a record triple product for stellarators was achieved [5].

Theoretical and gyrokinetic simulation studies suggest that ion-scale turbulence, in particular, ion temperature gradient (ITG) and trapped electron modes (TEM), are the primary transport relevant instabilities in the W7-X core plasma [6, 7], whereas transport by electron-scale instabilities is generally strongly reduced [8]. Validating these predictions against experimental measurements is important to understand the role of turbulence and to achieve high performance scenarios in W7-X and upcoming next generation devices like ITER. Various fluctuation diagnostics from the

plasma core to the scrape-off layer (SOL) are utilized on W7-X to identify and monitor broadband instabilities as well as coherent modes. Density and electron temperature fluctuation spectra (in both frequency and wavenumber space) of broadband turbulence can be used to identify and characterize the dominant turbulent instabilities that are expected to drive anomalous heat flux, such as ITG and TEM. For coherent modes, detection of energetic particle driven Alfvén modes can provide evidence for the existence of these particles and their impact on plasma performance.

The key core turbulence diagnostic is the newly completed phase contrast imaging (PCI) diagnostic [9], which has been designed, built and integrated into the project as a collaborative effort between the MIT Plasma Science and Fusion Center, the Max Planck Institute for Plasma Physics and SUNY Cortland.

The PCI diagnostic is a well-established tool for the measurement of density fluctuations in the core region of fusion plasmas [10–17]. Its principle [18] relies on the diffraction of a CO_2 laser beam on fluctuations of the plasma refractive index due to density fluctuations, which act as a phase grating for the laser beam. The diffracted and the direct component of the incident laser beam are spatially separated in the focal plane, where the phase of the direct component is delayed by $\pi/2$ by a phase plate, and the resulting laser intensity is proportional to the amplitude of the plasma density fluctuations. By imaging the beam onto an array of detectors, the wavenumber of the fluctuations is obtained. Since the diffracted components are related to the laser beam passing through the plasma, the detected intensity is independent of the time-averaged plasma density profile along the line of sight. The obtained plasma density fluctuation spectra in this base setup are line-integrated along the laser beam , providing amplitude and wavenumber of density fluctuations $I = \int_{l_1}^{l_2} \tilde{n}(\theta, t)\, \mathrm{d}l$, from which frequency-wavenumber spectra $S(k_\perp, f, \Delta r, t)$ are readily calculated.

Radial localization along the beam path is possible, depending on the geometry of the magnetic field. The fluctuations in toroidal magnetically confined plasmas are generally assumed to propagate nearly perpendicular to the local magnetic field. PCI is only sensitive to fluctuations propagating perpendicular to the laser beam due to its line-integration nature. Localized measurements along the beam are therefore possible because the component of the magnetic field perpendicular to the beam varies as a function of beam propagation distance. Fluctuations from different beam propagation distances scatter at rotationally different angles, which are projections of the local magnetic pitch angle onto a plane perpendicular to the PCI chords. At the focal plane of the PCI imaging system, these scattered beams appear at the corresponding angle, and thus can be selected by a rotational mask.

Current PCI systems on different tokamaks and stellarators are adapted to the specific requirements of the experiments they are used on. The PCI system on the TCV tokamak [16] has a laser beam path tangential to the magnetic surface. At the tangent point, PCI is only sensitive to fluctuations with a radial wavenumber, allowing it to achieve localized measurement using a selecting mask with excellent radial resolution ($\Delta\rho < 0.01$). On the LHD stellarator, the magnetic geometry corresponds to a large variation in pitch angle, allowing the PCI system [15] with a vertical laser beam path and a two-dimensional detector to resolve the measurement location along the beam. On the DIII-D tokamak, a combined PCI and heterodyne interferometer system [19] expands the measured fluctuation wavenumber to the low-k range to cover MHD modes.

The PCI setup at W7-X is outlined in detail in the following section. Beginning with the optical design in Sec. 2, we outline the selection of a suitable line of sight in Sec. 2.1, the selection of lasers

and associated beam conditioning optics before passage through the plasma in Sec. 2.2, and beam processing before detection on the receiving end in Sec. 2.3. Remote operation capabilities are required both for beam magnification adjustments (Sec. 2.4) and for alignment correction over the long optical path, and are detailed in Sec. 2.8. A feedback system that counteracts low frequency vibrations introduced by machine operation is described in Sec. 2.5. Section 2.6 describes the remotely operated rotating masks that act as spatial filters for radial selection of fluctuation signals. These operate on two independent beam paths which create the final image on two photoresistive detector arrays, detailed in Sec. 2.7. Finally, the continuous remote operation scheme by a web-based control system which ties in to the W7-X shot cycle, including online calibration and high capacity data acquisition, is described in Sec. 2.8. The entire system is calibrated with regard to amplitude and wavelength before every discharge using an acoustic speaker system in the beam path as introduced in Sec. 3. Exemplary results which illustrate the necessity and benefit of these features are summarized in Sec. 4, addressing the spectral characteristics of broadband turbulence and accompanying coherent Alfvénic modes.

2 Setup of the optical system

2.1 Port selection and diagnostic geometry

Due to the strong ballooning character of turbulence in tokamaks, PCI is usually set up to predominantly diagnose the outboard plasma cross section. In W7-X, however, regions of bad magnetic curvature exist also on the plasma inboard side. Therefore, one design requirement for the PCI laser beam was to cross the entire poloidal plasma cross section. Due to the lack of any central transformer solenoid, the PCI laser beam can principally exit the plasma on the inboard side. The long-pulse capability of W7-X with a specified maximum plasma pulse length of 30 min prohibits in-vessel mirrors due to the expected excessive heat loads. In addition, a monotonic magnetic field pitch angle variation along the beam path is desired for radial resolution of fluctuations with a spatial filtering mask (Section 2.6). The final selected ports (inboard: AEZ50, outboard: AET50) allow the laser beam passing the magnetic axis at a toroidal position of about 260.5°, which is 9.5° and 27.5° away from the nearest triangular and bean shaped plane, respectively.

The flux surface geometry and normal curvature at the toroidal angle of the beam intersection with the magnetic axis (ϕ = 260.5°) in the "standard" magnetic configuration of W7-X are shown in Fig. 1. At this toroidal location, the laser beam passes through bad curvature regions where ion-scale instabilities are expected to develop on both the outboard and inboard side.

Figure 2 shows the overall setup of the PCI diagnostic with two separate optical tables. On the first table, the laser beam is conditioned. The laser beam is sent upward along the inside of the torus towards the AEZ50 port. Two 9” steering mirrors located in the inboard mirror box redirect the beam first horizontally inside the box and then upward through the AEZ50 window at an 18° angle with respect to the horizontal plane. Outside the torus, another two 9” steering mirrors located in the outboard mirror box steer the beam coming out of the AET50 window first horizontally and then downward towards the second laser table where the detectors are housed. A sound wave speaker is installed inside the outboard mirror box between the two 9” steering mirrors for calibration. The total path length is about 22 m between the two optical tables.

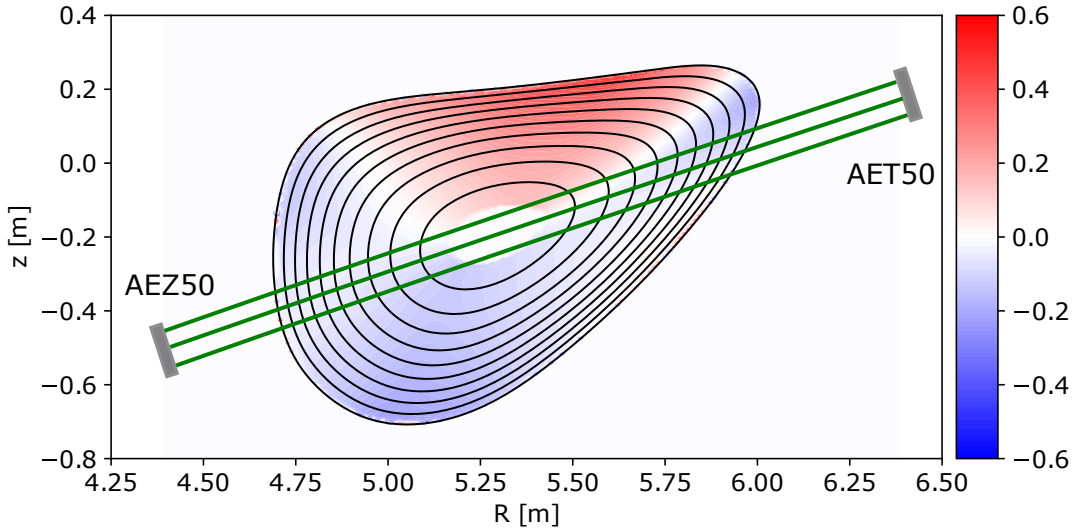

Figure 1. Poroidal cross-section of flux surfaces (black lines) and normal curvature (solid colors) in the standard magnetic configuration and probing beam lines of sight (green lines).

2.2 Laser table optical design

The laser optical table houses the lasers and prepares the beam for passage through the experiment. Its primary purposes are to magnify the probing infrared (IR) beam to its (variable) final diameter for plasma vessel passage, to remotely co-align the invisible IR beam with an additional visible pilot laser for alignment purposes, and to monitor the incident IR beam power and quality during operation.

The optical design of the laser table as calculated by the program Zemax© can be seen in Fig. 3. The probe laser beam of the PCI system is generated by a continuous wave (CW) 100 W, 10.6 μm infrared CO_2 laser (Synrad Firestar t60). The beam diameter at the laser output aperture is 2.2 mm with a 3.5 mrad beam divergence. A f = 500 mm lens is placed 350 mm in front of the laser aperture to reduce the Gaussian beam expansion. The resulting beam diameter is about 3.5 mm.

The beam then passes two 50% beam splitters and enters a telescope consisting of three ZnSe lenses: one plano-convex 1" diameter f = 200 mm lens (Thorlabs), one plano-concave 1" diameter lens f = −50 mm lens (Thorlabs), and one plano-convex 2" diameter f = 200 mm lens (II-VI Infrared). The magnification range of the telescope is about M = 0.8 to 4, resulting in a beam diameter ranging from about 2.8 mm to 15.7 mm after traversing 1500 mm on the optical table before entering the next telescope.

A 12 mW, 632.8 nm HeNe laser, Melles-Griot model, is combined with the IR beam to assist with alignment. The HeNe laser beam first passes through a fixed telescope consisting of a f = 150 mm and a f = 500 mm lens. An adjustable 3-lens telescope similar to the IR one is also used to expand the HeNe laser beam to the same size as the probe beam: one plano-convex 1" diameter f = 250 mm lens, one plano-concave 1" diameter lens f = −50 mm lens, and one plano-convex 2" diameter f = 250 mm lens. The magnification range is from M = 0.62 to 3.62 to

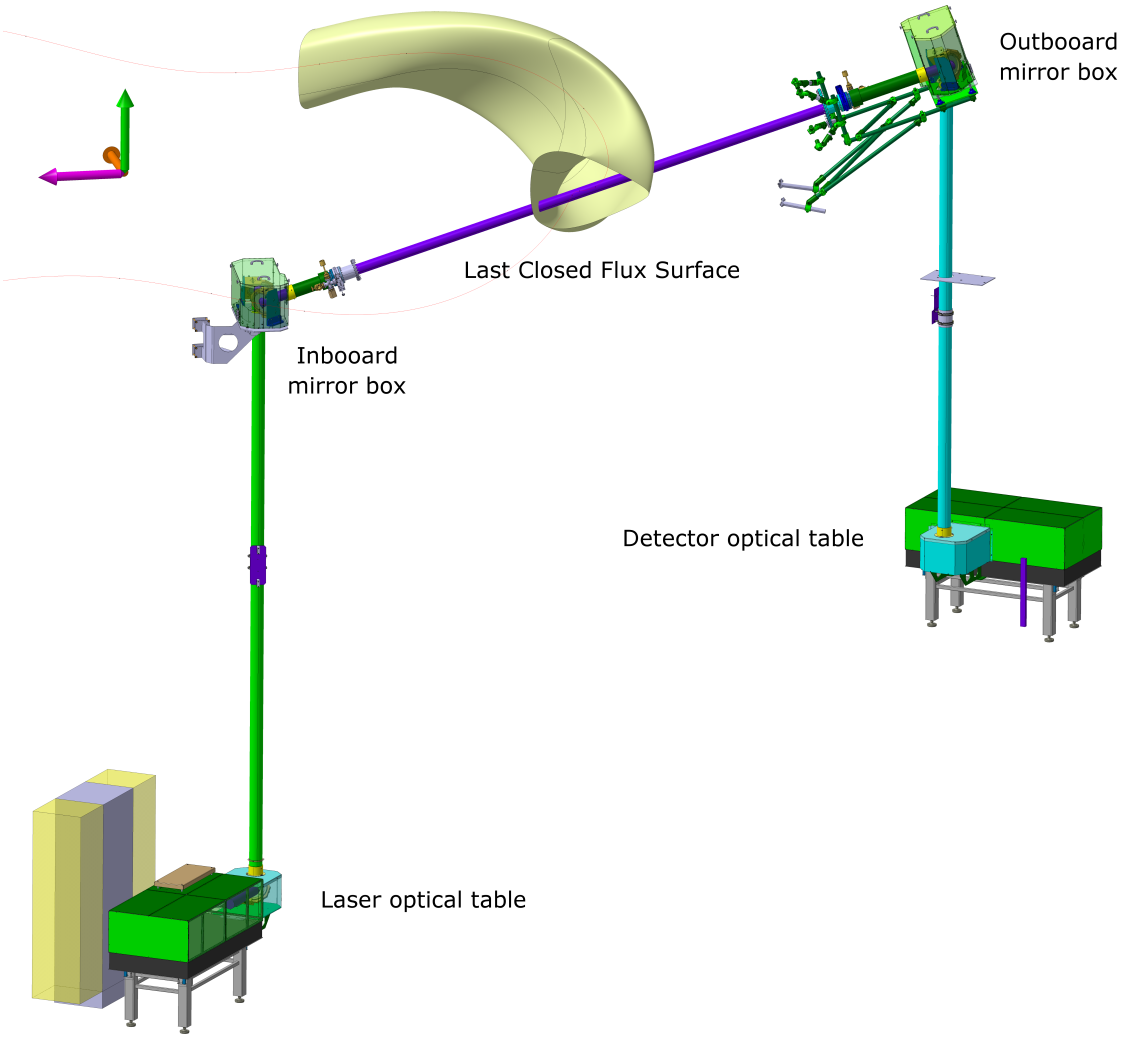

Figure 2. Overall setup of the PCI diagnostic

match up with the IR beam size. The two laser beams are then combined by a beam combiner.

While not illustrated in Fig. 3, two remote controllable flippable mirrors are installed between the beam combiner and the next optic. They are used to redirect the beam with different optical path lengths onto a thermal UV imaging plate for remote co-alignment checks.

The combined beams are then expanded with a telescope comprised of two off-axis parabolic (OAP) mirrors with a fixed magnification of $M = 80”/9” = 8.9$. The final beam size off the laser table can vary from 25 mm to 140 mm, and typically 80 – 100 mm is used.

2.3 Detector table optical design

The detector optical table houses the phase plate, detectors and associated beam manipulation hardware. Its purposes are: de-magnification of the beam to a manageable size and rotation of the image into the correct reference frame, active feedback control of the beam position, passage through the phase plate for phase contrast generation, beam power monitoring and verification of

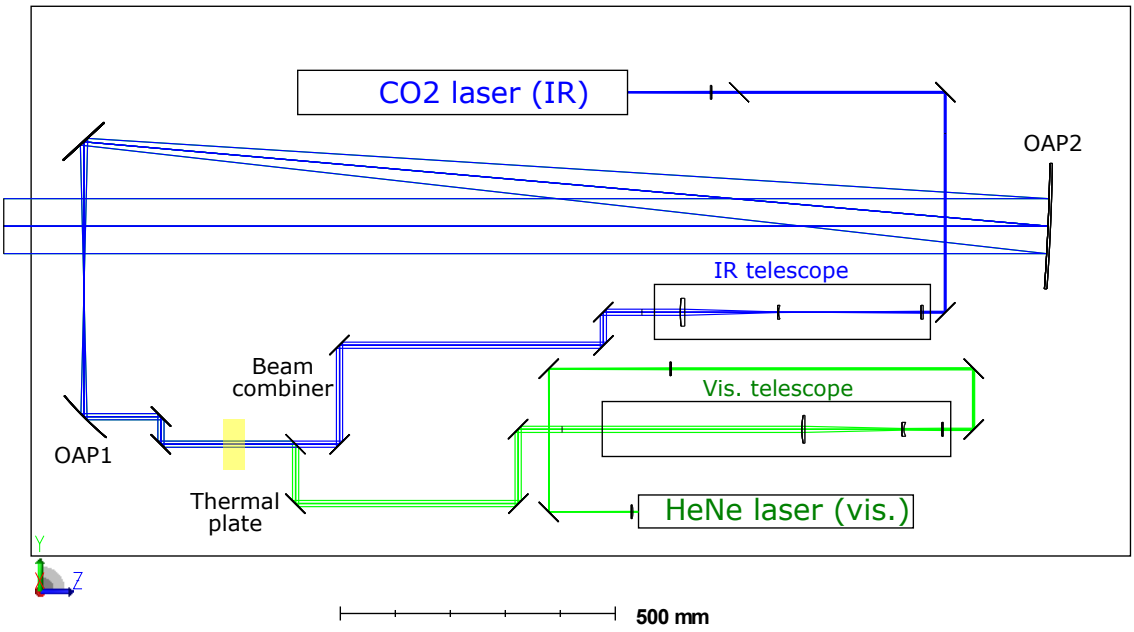

Figure 3. Optical design of the laser table. Blue and green lines represent the IR CO_2 and visible HeNe laser beam paths, respectively.

coalignment with the pilot laser, selection of probing range along the beam path by geometrical masking, and finally signal detection by the detectors.

Figure 4 shows the optical design of the detector table, in which the different colored rays represent the scattered beam from the center and the two edges. The returning laser beam is first mapped onto a large 9" diameter, 80" focal length OAP mirror, which focuses the beam onto the phase plate at its focal plane.

The converging beam is first sent through a beam rotator consisting of three plane mirrors, which ensures that the image of a plasma filament along the poloidal direction is aligned with the horizontal 1d detector array on the detector table. After the beam rotator, a steerable mirror reflects the beam onto a beam splitter which reflects 99% of the IR beam power onto the phase plate. A subsequent quadrature detector is installed behind the beam splitter. Its purpose is to form a feedback vibration compensation system (see section 2.5) with the steerable mirror to ensure a stable beam position on the phase plate. The reflected component of the beam from the phase plate is collimated by a 6" OAP mirror, which forms a telescope with a fixed magnification of $M = 6"/80" = 0.075$ with the large OAP mirror.

The phase plate (manufactured by Spire Semiconductor) is essentially a 2" gold plated mirror with a 1.1 mm wide groove crossing the center. The low-k diagnostic limit is then determined by the groove width to be $k_c = \pi d/\lambda f = 1.6$ cm^{-1}, where λ is the wavelength of the IR laser, $f = 80"$ is the focal length of the large OAP, and d is the groove width. The depth of the groove is $\lambda/8 = 1.325$ μm to create a $\pi/2$ phase shift between the unscattered and scattered components. The ZnSe material of the groove has a reflection coefficient of $\rho = 0.28$, which increases the signal

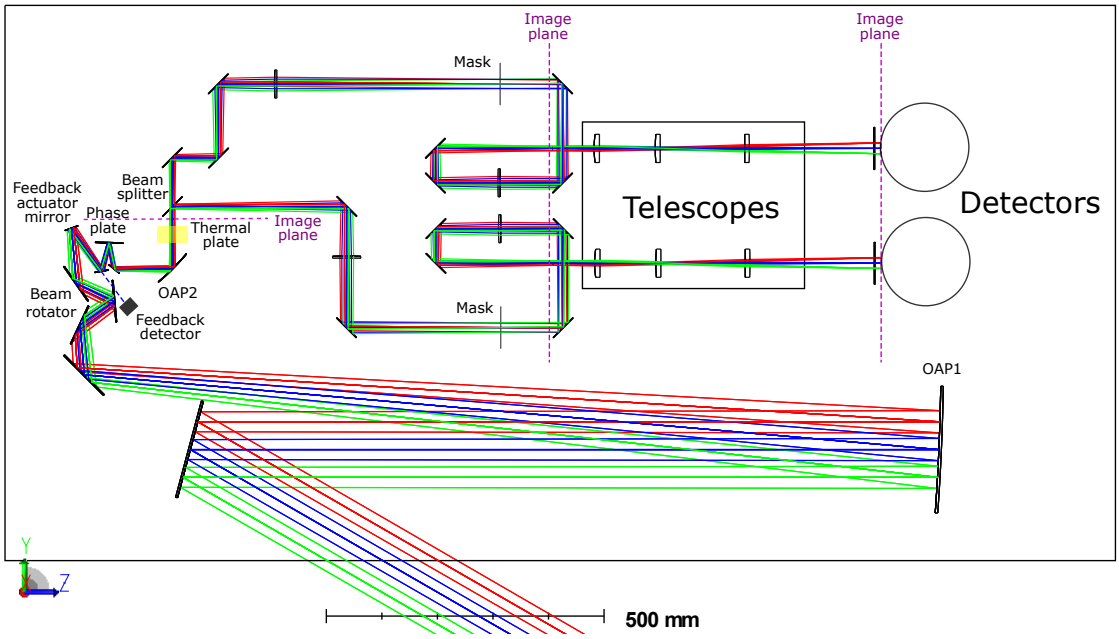

Figure 4. Optical design of the receiving table. Different colors represent the scattered rays from the center and two edges of the laser beam.

intensity by a factor $1/\sqrt{\rho} = 1.89$. A power meter behind the phase plate is used to measure the transmitted power through the phase groove, and of the entire optical system to this point.

A remote controllable flippable mirror is installed between the small OAP mirror and the next optic to redirect the beam to another thermal UV imaging plate for alignment and beam quality checks. The location of the flipping mirror is chosen so that the IR plate is located at the image plane created by the OAP telescope of the plasma in the vacuum vessel. This image plane is otherwise located right in front of the beam splitter without the flippable mirror.

The beam splitter sends the beam down to two separate beam paths. In each path, the laser beam first enters a $M = 1$ telescope with two 2" diameter, 16" focal length ZnSe lenses to create a second focal plane where the radial localization mask (section 2.6) is located, then passes through a remotely adjustable telescope which sets the detectable wavenumber range, and finally reaches the detector (section 2.7). The net magnification of the system is then equal to the product of the magnification of the OAP telescope (0.075) and the magnification of the adjustable telescope.

The $M = 1$ telescope creates a second image plane 16" after this telescope, 75 mm before the final adjustable telescope. This image plane acts as a virtual object plane which is imaged by the adjustable telescopes onto the detectors, with a wide range of magnification. The linear stages of the two telescopes are connected so that the magnifications are the same for the two detectors. Both telescopes consist of three plano-convex 2" diameter ZnSe lenses manufactured by Laser Research Optics, with focal lengths $f = 5$", 8.75" and 16", respectively. The magnification ranges from 1 to 5, which translates to a net magnification $M = 2.67$ to 13.33. This means the Nyquist wavenumber is from $k_N = 4.7$ to 23.5 cm^{-1} with 0.5 mm detector element spacing, which is sufficient to well

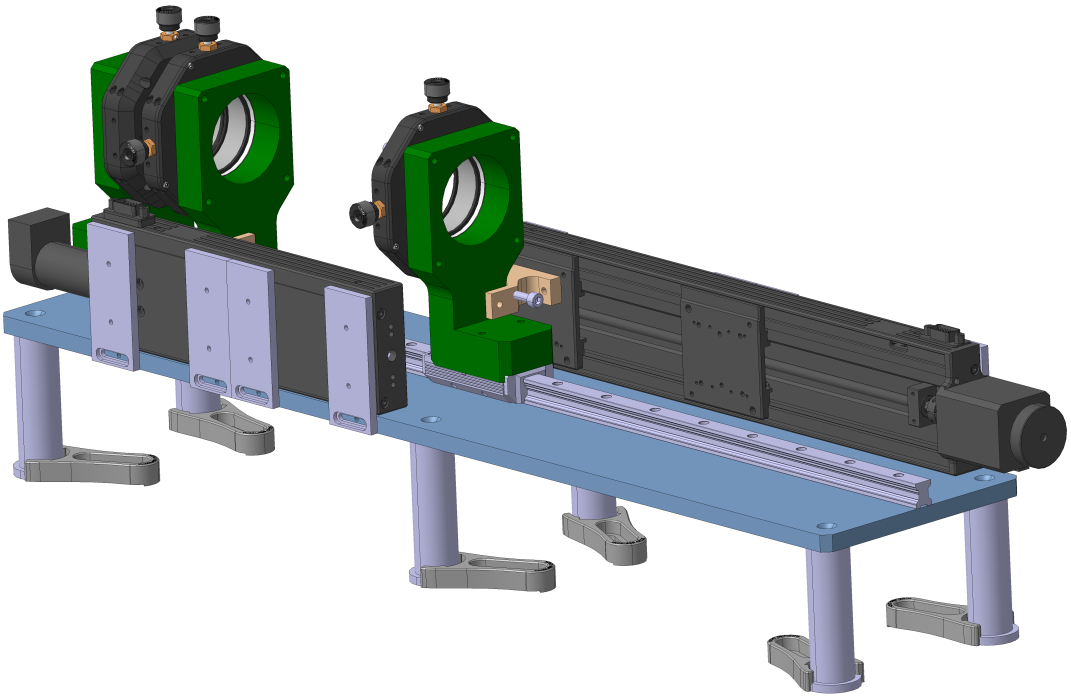

Figure 5. CAD view of the mechanical design of the motorized telescopes.

resolve ion-scale turbulence. In most discharges, the net magnification is set to 5, with the exception of late phase of the campaign, when the net magnification is set to be 3 to extend the wavenumber range for high-k fluctuations. It is worth noting that the magnification of the system is solely dependent on the detector table optics, and independent of the laser beam size.

2.4 Motorized telescopes

Remote operation requirements (see Sec. 2.8), both in terms of beam size and magnification selection and beam alignment, make a reliable adjustable telescope system indispensable. Optical calculations and lab tests show that very small perpendicular misalignments of the beams with regards to the lens center lead to significant optical aberrations and beam deflections, especially when using short focal length lenses required to fit all elements into a limited space. These are unacceptable especially on the transmitting table where the distance to the next observation point is about 1.5 m.

A total of 4 telescope systems (transmitting table IR and visible, both receiving table detectors) are used with the same mechanical design. Each of the three lenses is mounted in a cage system translating lens mount (Thorlabs CXY2) which allows for accurate co-alignment of lens centers. All three lenses are mounted on a precision sliding rail system which minimizes rotational motion perpendicular to the optical axis. These elements are shown in Fig. 5 together with the motorized linear stages (Physik Instrumente) which are mounted upright to save space and are coupled to the lens mounts via spring plunger screws. This design allows for reproducibility of lens positioning

at sub-mm precision, and lateral motion of the beam center on magnifications changes of around 1 mm per meter of throw distance.

2.5 Feedback system

It is essential to focus the unscattered beam component into the phase plate groove at all times in order to achieve phase contrast. Mechanical vibrations introduce excursions of the beam which result in a large noise signal on the detectors unrelated to plasma fluctuations, and in the worst case the unscattered beam could miss the groove, destroying the measurement signal altogether.

Therefore, a feedback vibration compensation system is used to keep the beam correctly focused. The system consists of a quadrant detector as the position sensor, an Arduino Due circuit board to calculate the feedback compensation signal, and a scanning mirror on a tip/tilt motor as the actuator.

The quadrant detector (Boston Electronics/VIGO PVMQ-10.6) is composed of four square detector elements, each with 1x1 mm^2 active area, with a spacing of $\sim$ 100 μm. The detector elements are protected behind a ZnSe window, and are connected with a QIP four-channel DC-coupled pre-amplifier with a 1 MHz high cutoff frequency. The detectors have a responsivity of $\sim$ 70 V/W with a bias current of 3.2 mA, a detectivity 1.7×10^7 $cmHz^{1/2}/W$, and 48 Ω resistance. The four-channel analog output voltage signals are directly proportional to the laser power on each detector, respectively.

The incoming laser beam delivered by the steerable feedback actuator mirror first passes through a beam splitter with 1% transmissivity for the infrared light and fully reflective for visible light before reaching the quadrant detector. The detector is installed 17 mm behind the beam splitter, where the Gaussian width of the beam is $\sim$ 1 mm with the largest beam size (140 mm).

An Arduino Due board is used to collect the output signals from the sensor and process them to produce two control signals that are sent to the actuator. The Due board was chosen because it has two channel analog output with a maximum 12-bit ADC/DAC and the possibility of hardware multi-threading, which allows remote user commands via ethernet. The response frequency is below 1 kHz. An operation amplifier is coupled with the board to expand the output voltage from $0.55 - 2.75$ V of the DACs to $1.65 - 8.25$ V required by the actuator. It is possible to remotely change the proportional gains of the feedback system, as well as the offsets in both directions. This means that the Arduino board can also be used to fine tune the laser position on the phase plate remotely in feedback-off mode. The two output control signals of the Arduino board are sent to a PI E-505 amplifier which provides the input voltage for the PI S-330.40L tip/tilt motor. A 0.5" silver mirror is attached to the motor to reflect the laser beam onto the beam splitter. The angular range of the motor is 7 mrad, which allows a $\pm$1 mm swing on the phase plate.

The feedback system has been so far tested in the laboratory without plasma operation. An extreme vibration case was tested by manually swiping the focused beam across the phase plate groove with remotely adding oscillating signals to the Arduino output offsets.

2.6 Radial localization masks

The variation of magnetic field direction and subsequently the scattered fluctuation direction along the laser beam is illustrated schematically in Fig. 6 for the "standard" magnetic configuration, in

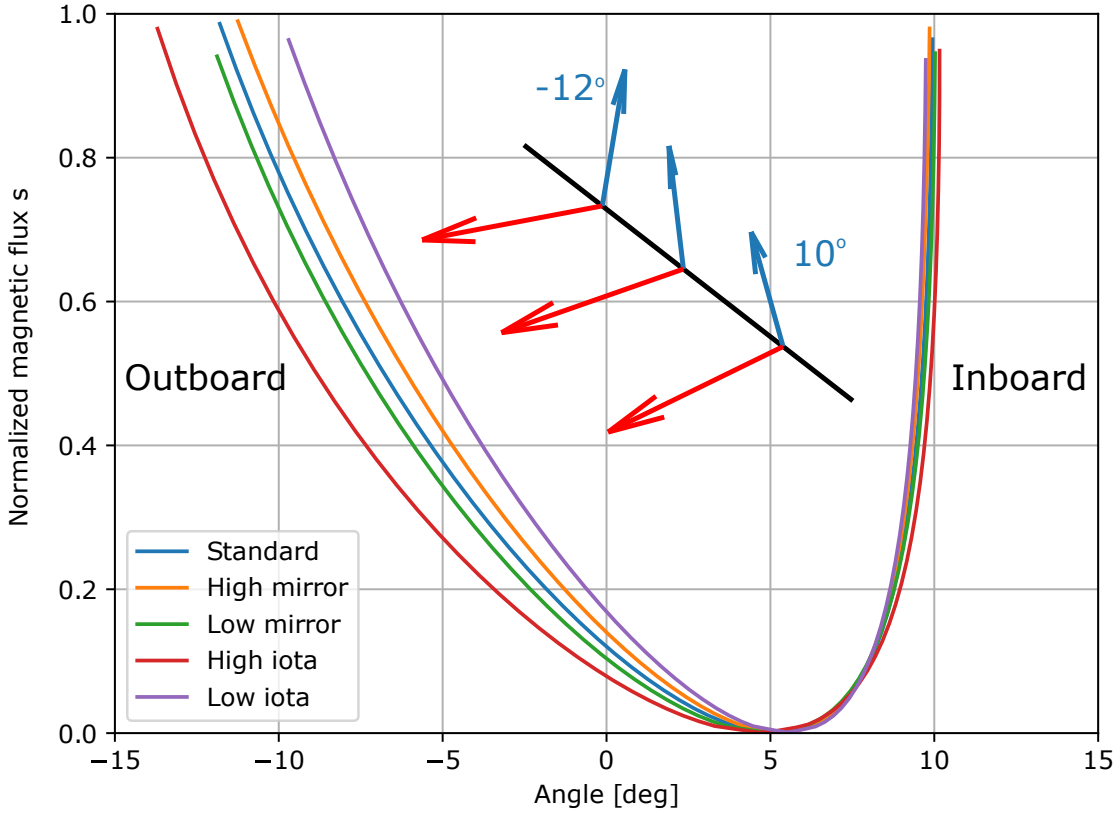

Figure 6. The corresponding radial location s in flux coordinate as a function of the fluctuation wavevector angle colored with different magnetic configurations. The reference angle is chosen at the center of the total angular variation (Inset). Schematic illustration of angular variation of the magnetic field (red), scattered density fluctuations (blue) along the PCI laser beam (black) from the inboard to outboard side with a "standard" magnetic configuration in W7-X.

which the total variation of the pitch angle is about 22 degrees. The reference angle ($\alpha = 0$) for the localization mask is chosen to be at the center of the 22 degree angular variation, instead of the scattering angle at the magnetic axis. The counter-clockwise direction when looking along the laser propagation in the vessel is chosen to be positive. The angle rotates clockwise, i.e., goes from positive to negative, from the inboard side to the outboard side.

The mask angle variation for different W7-X magnetic configurations is also shown in Fig. 6. The high and low mirror configurations are similar to the standard one, while the low and high iota configurations induce minimal and maximum variation due to the poloidal field strength, respectively. An asymmetry of the angle variation can be seen for all magnetic configurations, with only about 5 degrees between the magnetic axis and the inboard side plasma boundary and about 14 to 18 degrees to the outboard side plasma boundary.

The relatively small range of pitch angle variation requires an extremely narrow mask to achieve radially localized measurements. However, the focal spot of the laser beam has finite dimensions in practice, which limits the minimum angle of the mask. A 15° wedge-shaped mask was installed and

tested in plasma operation. The mask was rotated in the test from −30 degrees towards 30 degrees with 5 degree steps for repeated discharges. The test results show that the signal drops significantly when the mask angle is larger than ±20, where it is outside the plasma range. Differences in the shape of the $k - f$ spectra can also be observed with different mask angles, especially when switching between the inboard and outboard sides. The selection range is however inconclusive from the test, possibly due to the low alignment accuracy at the end of the campaign.

2.7 Dual detectors

The PCI system utilizes two photo-resistive detector arrays (Infrared Associates), which allows to perform radially localized measurements at two locations simultaneously with the two radial localization masks selecting different angles. Each detector array consists of 32 HgCdTe elements with 0.5 mm spacing, and is cooled in a liquid nitrogen filled dewar to reduce thermal noise. The detector photodiodes are AC-coupled to the pre-amplifier, model MCT-3200.

The frequency response of the detectors is calibrated with a modulated signal from an array of 114 OSRAM SFH 4059-QS LEDs operating at 0.86 μm. A Thorlabs PDA36A Si detector is used to calibrate the LED array response. The frequency response of the combined system of detector and pre-amplifier can be modeled as a band-pass filter with f_h and f_l as the high- and low-pass frequencies respectively:

$$H(f) = \frac{H_0}{\sqrt{(1 + f_h^2/f^2)(1 + f^2/f_l^2)}} \tag{2.1}$$

For all elements of both detectors, the high-pass frequency is around 2 kHz, and the low-pass frequency is 623 and 507 kHz, respectively. There is negligible phase delay observed between different detector elements. The absolute amplitude response can be neglected since this is achieved by a sound wave calibration.

2.8 Remote operation and data acquisition

The W7-X stellarator is equipped with superconducting magnetic coils. Operational constraints will severely limit access to the diagnostic during future campaigns to eventually once a week, which makes remote operation central to the diagnostic design.

The main goals of the remote operation are:

1. Check and align both the IR and visible laser remotely against the drift of the laser beam during the operation.

2. Modify the beam size and system magnification for measuring different ranges of wavenumbers via the telescopes described in Sec. 2.4 of both the visible pilot and IR beams.

3. Rotate the spatial filtering mask to select different radial ranges.

At selected observation points, the visible beam can be observed (and is automatically documented in each discharge) with video cameras by either imaging onto a screen which is remotely flipped into the beam path (after the beam combiner on the laser table and before the beam splitter on the detector table) or by directly observing the laser spot on the mirror. These are used for remote alignment through the entire system, including passage through the plasma vessel. Piezo-driven

mirror mounts (Physik Instrumente) allow for 2-axis positioning of selected mirrors to center the beam on crucial components and through both port windows. These mirrors include the ones between the telescope and the beam combiner for co-alignment on the laser table, the ones before and after the $M = 1$ telescope lenses on the detector table, as well as the 9" mirrors inside the mirror box. The port windows have symmetrical posts installed which cast shadows onto a screen on the receiving table for beam centering, since direct observation is not possible at the windows due to space constraints.

After the visible beam alignment, the IR beam is coaligned with it using thermal UV imaging plates which are also observed by cameras. By varying the throw distance onto the plate using two flippable mirrors and alternating between the visible and IR beams, the IR beam is successively coaligned using two steerable mirrors. Minor adjustments are required due to thermal expansion of components throughout an experimental day, and after magnification changes of the telescopes.

Alignment changes and system observation is done through an integrated remote control system available to the diagnostic operator through a GUI. The motor drives for telescopes and steering mirrors, laser controllers, screen flippers and UV imaging plates together with the video cameras and laser power meters are implemented in a common framework. This allows for complex tasks such as switching between observation points by moving flippers, adjusting IR laser power to avoid damage to components and determining a safe system state at all times. Furthermore, the system manages the shot cycle including laser warm-up and sound wave calibration (see Sec. 3), and automatically documents key alignment information before each discharge by saving images of selected screens, power meter values and all optical element positions.

Data acquisition of the amplified detector signals is done by 32-channel digitizers (DTACQ ACQ480) at typically 2 MS/s and locked to the experimental master clock, with a capacity of 8 GB which corresponds to a total duration of 62.5 s. The digitizers support gated triggering, which allows for flexible selection of data acquisition intervals within the long pulses of W7-X (up to 100 s).

3 Wavenumber and Amplitude Calibration

The diagnostic contains a sound wave calibration system. Before every discharge, an ultrasonic sound wave is launched by a speaker in air through which the laser passes after leaving the vacuum vessel. The speaker is mounted inside the outboard mirror box in between the two 9" mirrors, adjusted so that the sound wave propagates through the laser beam at an angle parallel to plasma fluctuations in the center of the total variation range. This propagation direction is aligned with the 1d detector array after the laser passes through the beam rotator, as described in section 2.3. The inside of the mirror box lid is covered by sound-absorption materials to minimize sound wave reflection.

A series of sound wave bursts at a range of frequencies is generated by a Fostex FT17H speaker, of which the $f = 20$ kHz, $k = 3.7$ cm^{-1} one is typically used for evaluation. The pressure fluctuations of known frequency, wavenumber and amplitude induce a phase of the laser beam analogous to plasma density fluctuations and therefore generate a similar PCI signal [20].

Figure 7 shows an example of a sound wave measurement. The sound wave is launched at 0 ms and reaches the laser beam at 0.5 ms, as it propagates through the laser the image propagates along

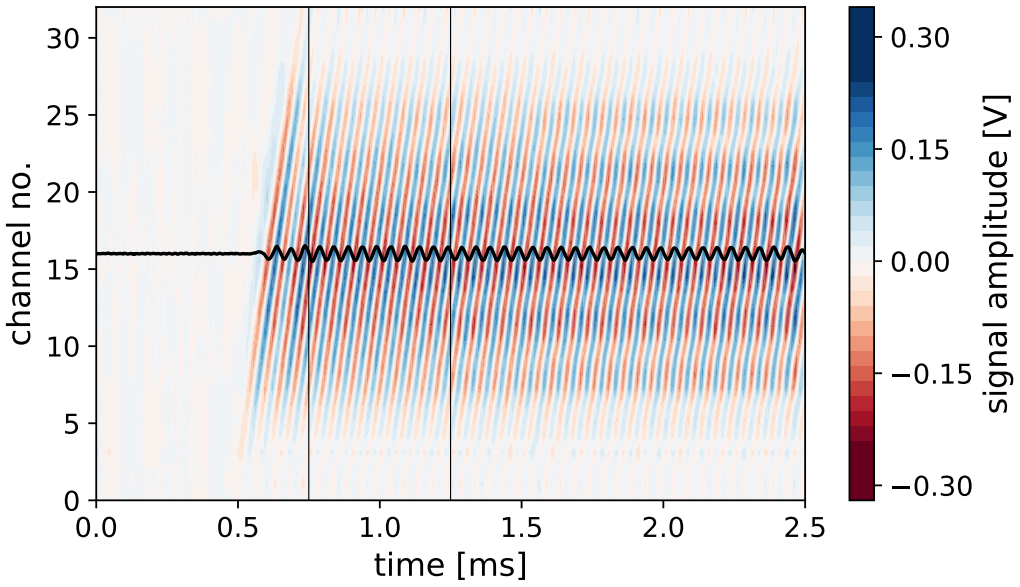

Figure 7. PCI measurement of a 20 kHz sound wave. The vertical lines mark the start (0.75 ms) and end (1.25 ms) of the time window which is used for the calculation of the fluctuation amplitude.

the detector array. The difference of fluctuation amplitude on different detector channels is due to the finite size and Gaussian shape of the laser spot on the detector array. 1.25 ms after the launch, a reflected wave arrives back at the laser beam and causes a standing wave pattern.

3.1 Calibration of magnification

The net magnification of the optical system on the receiving side of the diagnostic can be examined by comparing the known wavenumber of the sound wave to the wavenumber measured at the detector. The wavenumber-spectrum at the respective sound wave frequency shows a peak at the wavenumber of the sound wave. When searching for a maximum in the wavenumber-spectrum, a cubic spine interpolation is used to improve the limited wavenumber resolution. Figure 8 shows an example of a wavenumber-frequency-spectrum of a sound wave at two different frequencies.

The magnification, m, is calculated as

$$m = \frac{k_{\text{det}}}{k_{\text{sound}}} = \frac{k_{\text{det}} c_{\text{sound}}}{2\pi f_{\text{sound}}}, \tag{3.1}$$

with wavenumber of the sound wave, k_{sound}, the wavenumber of the image at the detector, k_{det}, the speed of sound, c_{sound}, and the sound wave frequency, f_{sound}. The magnification obtained in the calibration process matches the theoretical value set by the OAP telescope and the adjustable telescopes on the detector table (sections 2.3 and 2.4) well and confirms that the intended magnification was achieved. Figure 9 shows the fluctuation amplitude profile on the detector array for two discharges with different magnifications of the receiving side telescopes. The width of the profile increases for a lower magnification (#180904021: $m = 5$, #181004028: $m = 3$). Accordingly, the intensity measured at the detector decreases for lower magnification. However, the amplitude of

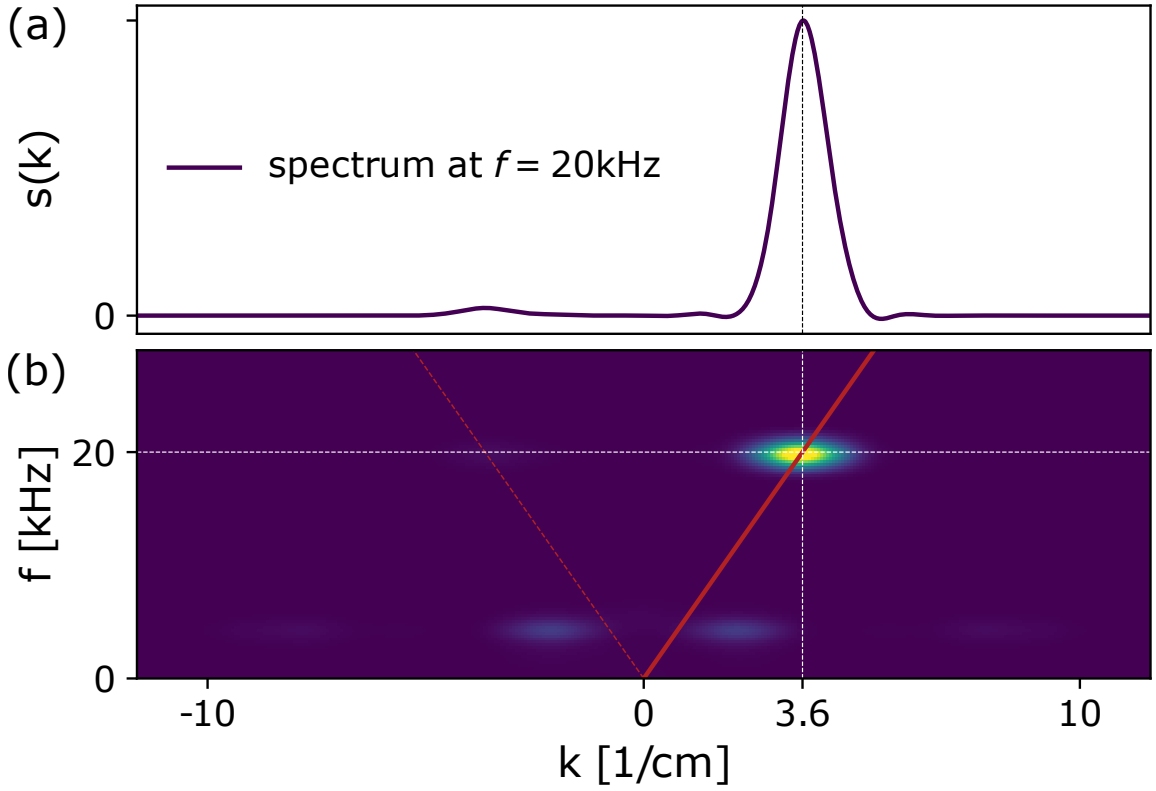

Figure 8. Wavenumber-frequency-spectrum of a $f = 20$ kHz sound wave. The wavenumber-spectrum at the respective sound wave frequency, which is used to determine the wavenumber of the sound wave, is shown above the wavenumber-frequency-spectrum. The red lines illustrate the sound speed. The sound wave propagates in positive k direction (solid red), and the reflected wave in the opposite direction (dashed red).

the sound wave pressure should remain the same. A calibration of fluctuation amplitude needs to be included to correct this as well as other effects such as misalignment and laser power variations.

3.2 Calibration of fluctuation amplitude

The sound wave pressure fluctuations, $\tilde{p}$, can be related to electron density fluctuations, $\tilde{n}_e$, causing the same signal via [20]

$$\int \tilde{n}_\mathrm{e}\,\mathrm{d}l = \frac{2\pi(N_0 - 1)}{\lambda_\mathrm{laser}^2 r_\mathrm{e}\gamma p_0}\int \tilde{p}\,\mathrm{d}l, \tag{3.2}$$

with reference refractive index, N_0, wavelength of the laser, λ_laser, classical electron radius, r_e, heat capacity ratio, γ, and reference air pressure, p_0. The sound field of the speaker was measured with a calibrated microphone by Piezoelectronics (PCB Teds 378C01) in order to obtain $\tilde{p}$. Integration at the height of the center of the laser beam yields $\int \tilde{p}\,\mathrm{d}l$.

For a consistent sound wave amplitude measurement the fluctuation amplitude profile on the detector array is analysed. Examples are shown in Fig. 9. The position of the center may vary due to small changes in alignment and the amplitude may change due to the same reason, changes in magnification or laser related variations. The profiles of the sound wave measurements must match with the profiles during plasma operation reasonably well for a valid calibration. A narrow time

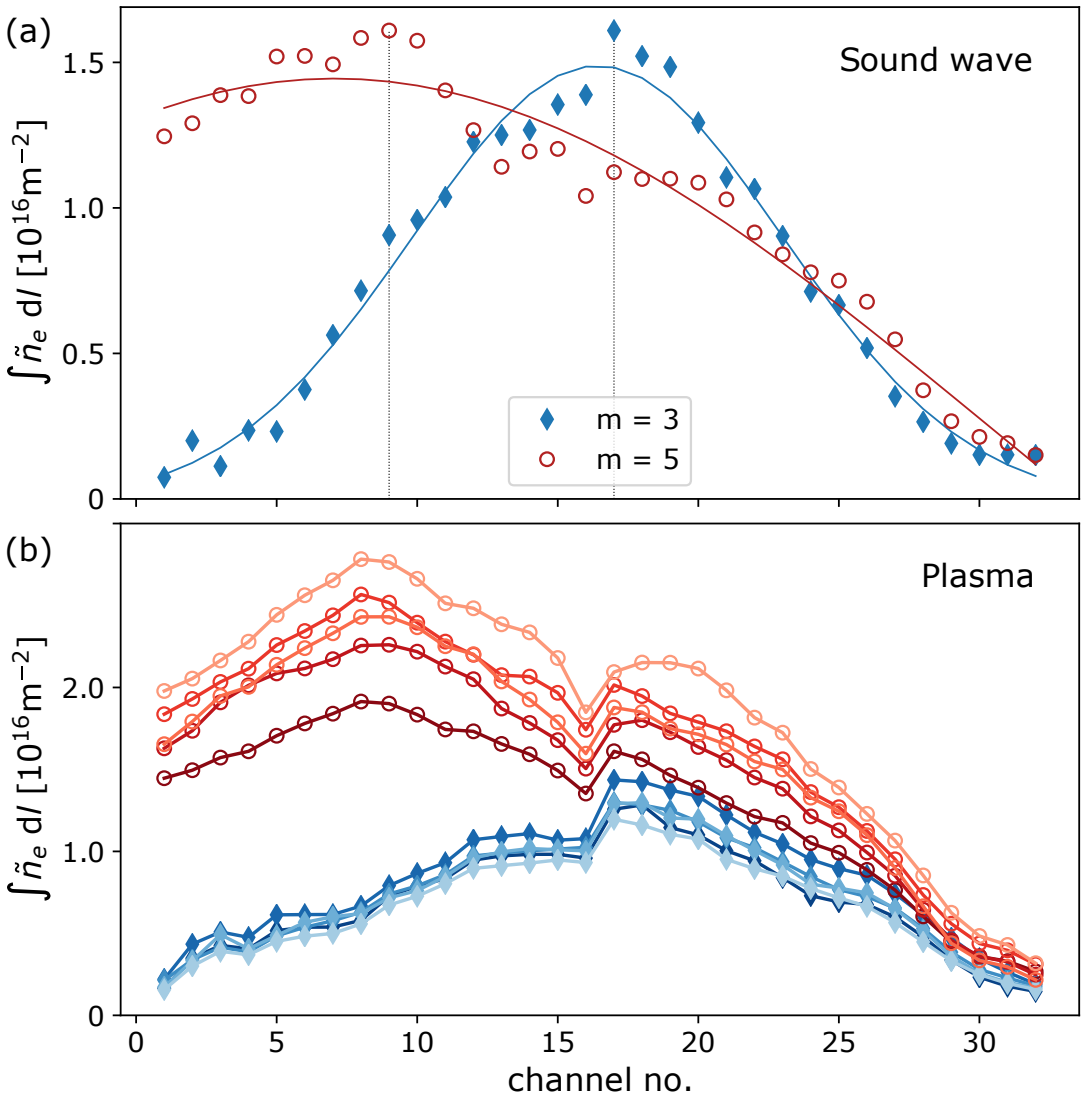

Figure 9. Fluctuation amplitudes of sound wave (a) and plasma density (b) for two discharges with net magnification $m = 3$ and 5, respectively. A Gaussian function was fitted to the data of the sound wave (dashed lines). 5 time points during the plasma discharge were chosen for each discharge (increasing transparency). The vertical lines in the top plot mark the amplitude maxima, which were used for calibration.

window is chosen for the analysis (see Fig. 7) in order to avoid measuring a standing wave pattern induced by a reflected wave, which distorts the amplitude profile.

In order to select the amplitude at the center of the laser, the maximum of the profile is chosen as marked in Fig. 9. Additionally, a Gaussian function is fitted to the profile as a criterion for the quality of the profile. If the fit has a large error or the center of the Gaussian deviates significantly from the position of the maximum, the profile is distorted (e.g. due to misalignment), which introduces a systematic error to the calibration. The maximum fluctuation amplitude together with the value for $\int \tilde{n}_e \, dl$ obtained from equation (3.2) is used to calibrate the fluctuation amplitude

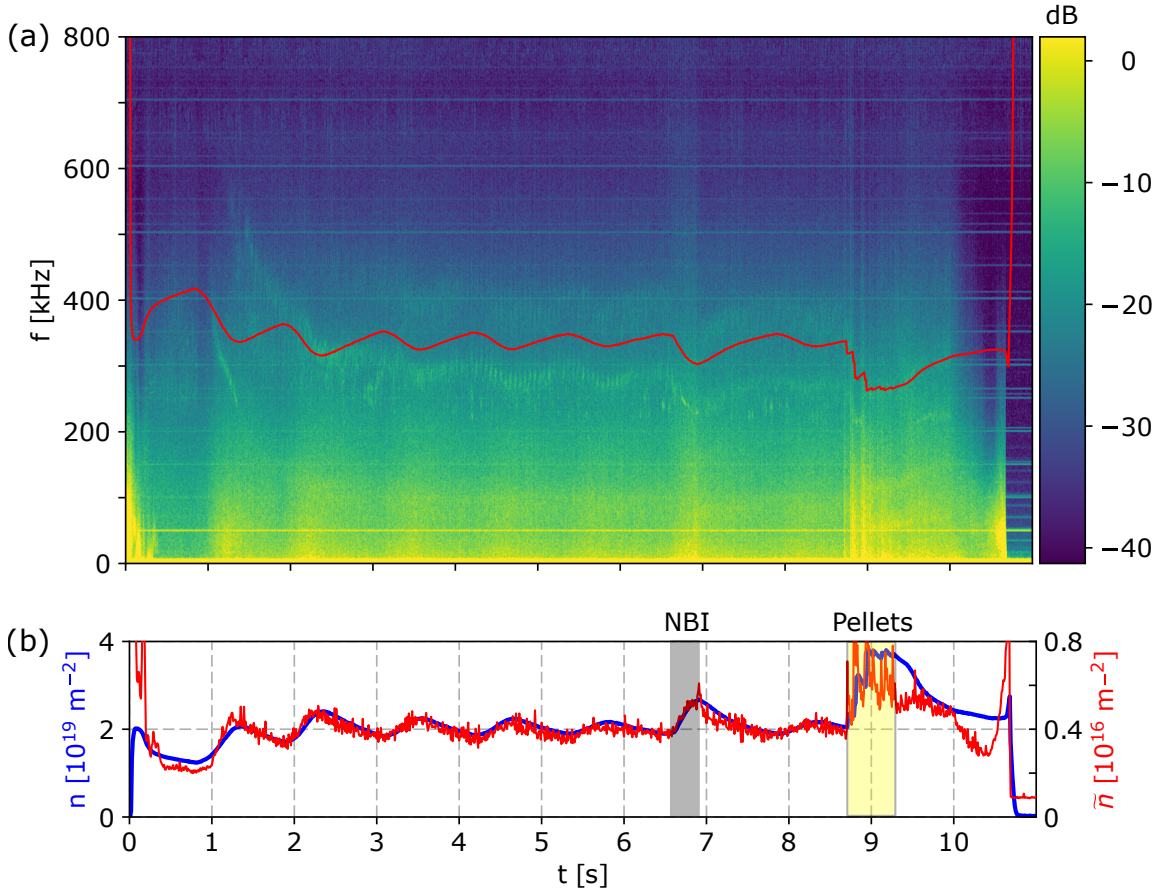

Figure 10. Overview of W7-X program XP20180822.017. Top: Frequency spectrogram of PCI showing the broadband density fluctuations and several coherent mode. The red line indicates the theoretical Alfvén frequency; bottom: line-integrated density and density fluctuations measured by interferometer and PCI, respectively.

measured by the same channel during plasma measurements.

4 Density fluctuations in Wendelstein 7-X

The PCI system on W7-X has been run successfully for two operation campaigns from 2017-2018, and in this time has reliably and continuously acquired data for most discharges. It has been a central tool for continuously monitoring density fluctuations and providing feedback on favorable conditions regarding improved confinement at reduced turbulence levels.

Figure 10 (a) shows a frequency spectrogram of density fluctuations measured by a single line-of-sight of the PCI diagnostic. The turbulent spectrum is broadband and its power decays exponentially towards high frequencies. An oscillation of the fluctuation amplitude can be observed, especially in the low frequency range ($f < 300$ kHz), this is mainly due to the oscillation in bulk plasma density as shown in Fig. 10 (b). Here the line-integrated plasma density (blue line) is measured by an interferometer diagnostic. The density fluctuations amplitude is calculated by integrating the spectrogram in Fig. 10 (a) over the frequency range 10 – 1000 kHz. The low

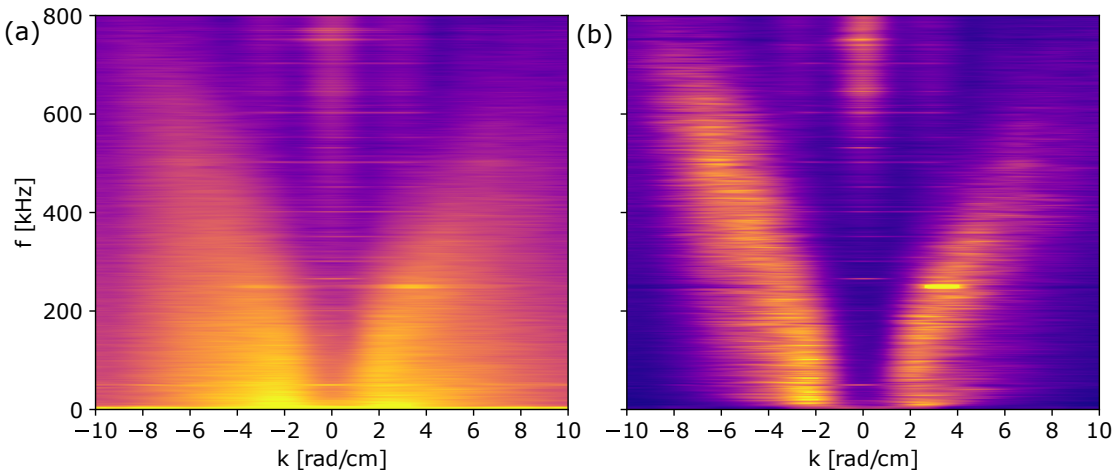

Figure 11. Frequency-wavenumber spectra of density fluctuations (a) without normalization (b) frequency-normalized, respectively.

frequency component $f < 10$ kHz is omitted to avoid noises from the laser. An additional 3 MW NBI heating from $t = 6.6$ to 6.9 s and a series of cryogenic pellet injections from $t = 8.7$ to 9.3 s both induce changes in the fluctuation spectrum. The density fluctuation amplitude scales well with the line-integrated density throughout the discharge up to the pellet injection, including the NBI phase. In a transient phase after pellet injection from $t = 9$ to 9.6 s, a drop in the fluctuation amplitude compared to the plasma density can be observed. This temporary reduction of turbulence is believed to be the main reason for the transient boost in confinement post pellets [4].

Coherent modes in the range of several hundreds of kilohertz can also be observed in the spectrum. They are thought to be Alfvénic in nature due to the correlation with the Alfvén frequency that is inversely proportional to the square root of density, indicated by the red line in Fig. 10 (a). It is noted that the theoretical Alfvén frequency is calculated from the line-integrated density, which is not the local plasma density where the Alfvén modes were developed. Therefore, it is only used as an indication of the frequency evolution, but not necessarily fits exactly with the observed mode frequency. These Alfvénic modes were frequently observed by the PCI diagnostic even though most plasma were produced and maintained purely with ECH and thus absent of energetic-ions. This is also suggested by the fact that these modes could only be observed in low density plasmas, typically with line-integrated density below 6×10^{19} m^{-2}. It has been suggested that they are excited by the thermal electron population or energetic trapped electrons [21].

Figure 11 (a) shows the frequency-wavenumber spectrum $S(k, f)$ of density fluctuations during the NBI phase in the discharge, measured from all 32 line-of-sights of PCI. The spectra are generally broadband in both the frequency and wavenumber domain, with its power decays exponentially towards high frequency and wavenumber. Most fluctuation power is at ion scales with $k\rho_s \leq 1$, which is about $k \approx 4$ cm^{-1} with typical temperature around 1 keV. A low-k cutoff can be observed at $k_c = \pm 1.6$ cm^{-1}, which is determined by the width of the phase plate groove (see Sec. 2.3). The two-sided nature of the spectra is due to the line-integrated measurement: fluctuations with their wavevectors in a single poloidal direction appear as if propagating in two opposite directions,

one originating from the inboard side and the other from the outboard side. Figure 11 (b) shows the spectra normalized to unity at each frequency. It is apparent that the broadband fluctuations propagate around two phase velocities in two opposite directions, which is identified as the $E \times B$ drift velocity. For ion-root plasmas in W7-X, the radial electric field is negative at the edge of confined region where drift-wave instabilities are expected to develop, which leads to a downward $E \times B$ drift at the outboard side and upward at the inboard side. It is known from the sound wave calibration that upward propagating fluctuations such as the sound wave have positive k (see Fig. 8), therefore the positive and negative k branch of broadband fluctuations are identified as originating from the inboard and outboard side, respectively.

The Alfvénic mode can be observed to be coherent in both frequency and wavenumber domain. Here the sign and value of the mode wavenumber does not necessarily indicate its propagating direction or mode number. It has been previously shown [22] that the mode can be attributed to integration through regions of positive and negative density fluctuations of the Alfvénic modes in the deep core which tend to cancel and create a complex pattern of peaks and nodes.

5 Conclusion

The PCI diagnostic is a powerful new diagnostic providing measurements of turbulent density fluctuations and coherent modes. The diagnostic has been continuously and reliably operated for two W7-X operation campaigns from 2017-2018. The system allows remote operation and adjustments, as well as automatic calibration and documentation. As the only core fluctuation diagnostic in W7-X at this stage, it has been the key contributor to analysis of high performance discharges by providing measurements which have shown a reduction of turbulence accompanied with improved confinement. Its ability to provide a complete turbulence spectrum in both frequency and wavenumber space, as well as absolutely calibrated density fluctuations, allows detailed comparison to gyrokinetic turbulence simulations.

Acknowledgement

This work is partly sponsored by the US Department of Energy, Office of Fusion Energy Sciences under grant number DE-SC0014229. This work has been carried out within the framework of the EUROfusion Consortium and has received funding from the Euratom research and training programme 2014-2018 and 2019-2020 under grant agreement No 633053. The views and opinions expressed herein do not necessarily reïňĆect those of theEuropean Commission.

References

[1] Grieger G, Lotz W, Merkel P, Nührenberg J, Saper J, Strumberger E, Wobig H, Burhenn R, Erckmann V, Gasparino U, Giannone L, Hartfuss H J, Jaenicke R, Kühner G, Ringler H, Weller A and Wagner F 1992 *Physics of Fluids B: Plasma Physics* **4** 2081

[2] Wolf R C, Alonso A, Äkäslompolo S, Baldzuhn J, Beurskens M, Beidler C D, Biedermann C, Bosch H S, Bozhenkov S, Brakel R, Braune H, Brezinsek S, Brunner K J, Damm H, Dinklage A, Drewelow P, Effenberg F, Feng Y, Ford O, Fuchert G, Gao Y, Geiger J, Grulke O, Harder N, Hartmann D,

Helander P, Heinemann B, Hirsch M, Höfel U, Hopf C, Ida K, Isobe M, Jakubowski M W, Kazakov Y O, Killer C, Klinger T, Knauer J, König R, Krychowiak M, Langenberg A, Laqua H P, Lazerson S, McNeely P, Marsen S, Marushchenko N, Nocentini R, Ogawa K, Orozco G, Osakabe M, Otte M, Pablant N, Pasch E, Pavone A, Porkolab M, Sitjes A P, Rahbarnia K, Riedl R, Rust N, Scott E, Schilling J, Schroeder R, Stange T, von Stechow A, Strumberger E, Pedersen T S, Svensson J, Thomson H, Turkin Y, Vano L, Wauters T, Wurden G, Yoshinuma M, Zanini M, Zhang D and the Wendelstein 7-X Team 2019 *Physics of Plasmas* **26** 082504

[3] Bozhenkov S, Kazakov Y, Ford O, Beurskens M, Alcuson J A, Alonso J, Baldzuhn J, Brandt C, Brunner K, Damm H, Fuchert G, Geiger J, Grulke O, Hirsch M, HÃűfel U, Huang Z, Knauer J, Krychowiak M, Langenberg A, Laqua H, Lazerson S, Marushchenko N, Moseev D, Otte M, Pablant N, Pasch E, Pavone A, Proll J, Rahbarnia K, Scott E, Smith H, Stange T, von Stechow A, Thomsen H, Turkin Y, Wurden G, Xanthopoulos P, Zhang D, Wolf R and the Wendelstein 7-X Team 2020 *Nuclear Fusion* **60** 066011

[4] v Stechow A, Grulke O, Wegner T, Proll J H E, Alcuson J, Smith H, Xanthopoulos P, Beidler C, Beurskens M, Bozhenkov S, Edlund E, Geiger B, Huang Z, Ford O, Fuchert G, Langenberg A, Pablant N, Pasch E, Porkolab M, Rahbarnia K, Schilling J, Scott E, Vanó L, Weir G and the Wendelstein 7-X Team Suppression of core turbulence by proïňĄle shaping in wendelstein 7-x submitted to Physical Review Letters

[5] Baldzuhn J, Damm H, Beidler C D, McCarthy K, Panadero N, Biedermann C, Bozhenkov S A, Brunner K J, Fuchert G, Kazakov Y, Beurskens M, Dibon M, Geiger J, Grulke O, Höfel U, Klinger T, Köchl F, Knauer J, Kocsis G, Kornejew P, Lang P T, Langenberg A, Laqua H, Pablant N A, Pasch E, Pedersen T S, Ploeckl B, Rahbarnia K, Schlisio G, Scott E R, Stange T, von Stechow A, Szepesi T, Turkin Y, Wagner F, Winters V, Wurden G, Zhang D and the Wendelstein 7-X Team 2019 *Plasma Physics and Controlled Fusion* **61** 095012

[6] Proll J H E, Helander P, Connor J W and Plunk G G 2012 *Physical Review Letters* **108** 245002

[7] Xanthopoulos P, Plunk G, Zocco A and Helander P 2016 *Physical Review X* **6** 021033

[8] Plunk G G, Xanthopoulos P, Weir M, Bozhenkov A, Dinklage A, Fuchert G, Geiger J, Hirsch M, Hoefel U, Jakubowski M, Langenberg A, Pablant N, Pasch E, Stange T, Zhang D and the W7-X Team 2019 *Physical Review Letters* **122** 035002

[9] Edlund E M, Porkolab M, Huang Z, Grulke O, Böttger L G, von Sehren C and von Stechow A 2018 *Review of Scientific Instruments* **89** 10E105

[10] Weisen H 1988 *Review of Scientific Instruments* **59** 1544

[11] Coda S and Porkolab M 1992 *Review of Scientific Instruments* **63** 4974

[12] Coda S 1997 *An Experimental Study of Turbulence by Phase-Contrast Imaging in the DIII-D Tokamak* Ph.D. thesis Massachusetts Institute of Technology

[13] Lin L, Edlund E M, Porkolab M, Lin Y and Wukitch S J 2006 *Review of Scientific Instruments* **77** 10E918

[14] Porkolab M, Rost J C, Basse N, Dorris J, Edlund E, Lin L, Lin Y and Wukitch S 2006 *IEEE Transactions on Plasma Science* **34** 229

[15] Tanaka K, Michael C A, Vyacheslavov L N, Sanin A L, Kawahata K, Akiyama T, Tokuzawa T and Okajima S 2008 *Review of Scientific Instruments* **79** 10E702

[16] Marinoni A, Coda S, Chavan R and Pochon G 2006 *Review of Scientific Instruments* **77** 10E919

[17] Gong S B, Yu Y, Xu M, Jiang W, Zhong W L, Shi Z B, Wang H J, Wua Y F, Yuan B D, Lan T, Ye M Y, Duan X R and the HL-2A team 2017 *Fusion Engineering and Design* **123** 802

[18] Zernike F 1934 *Physica* **1** 689

[19] Davis E M, Rost J C, Porkolab M, Marinoni A and Zeeland M A V 2018 *Review of Scientific Instruments* **89** 10B106

[20] Mazurenko A 2001 *Phase Contrast Imaging on the Alcator C-Mod tokamak* Ph.D. thesis Massachusetts Institute of Technology

[21] Windisch T, Krämer-Flecken A, Velasco J L, Könies A, Nührenberg C, Grulke O, Klinger T and the W7-X team 2017 *Plasma Physics and Controlled Fusion* **59** 105002

[22] Edlund E M, Porkolab M, Kramer G J, Lin L, Lin Y and Wukitch S J 2009 *Physical Review Letters* **102** 165003